Earth and Planetary Science Letters 525 (2019) 115753

Contents lists available at ScienceDirect

Earth and Planetary Science Letters

www.elsevier.com/locate/epsl

Theoretical studies on the hydrous lower mantle and D″ layer minerals

Jiajun Jiang [a,b], Feiwu Zhang [a,*]

[a] State Key Laboratory of Ore Deposit Geochemistry, Institute of Geochemistry, Chinese Academy of Sciences, Guiyang 550081, China
[b] University of Chinese Academy of Sciences, Beijing 100049, China

ARTICLE INFO

Article history:
Received 27 April 2019
Received in revised form 25 July 2019
Accepted 1 August 2019
Available online xxxx
Editor: J. Brodholt

Keywords:
hydrogen
bridgmanite
post-Perovskite
phase transition
elasticity property
first-principal

ABSTRACT

The incorporation mechanisms and elastic properties of hydrous Bridgmanite (Brg) and post-Perovskite (PPv) are investigated by using first principles calculations at the lower mantle pressures. The elastic properties calculations in both (Al, Fe)-free and (Al, Fe)-bearing systems give evidences that hydrogen has less effect on the elastic wave velocities and moduli in (Al, Fe)-free and Al-bearing system. However, the elastic wave velocities and moduli, especially the shear velocity V_S and the shear modulus G, are remarkably sensitive to the presence of hydrogen in the Fe-bearing system. The calculated shear velocity anomaly (dV_S) are −2.9% for $Fe^{3+}{}_{Si}H$-Brg and −3.1% for $Fe^{3+}{}_{Si}H$-PPv, which are very close to the average anomaly value of LLSVPs. This result may imply the Ferric-bearing hydrous $MgSiO_3$ is likely a dominated mineral in LLSVPs. Density functional perturbation theory (DFPT) and QHA calculation have also been performed to determine the P–T phase diagram for different hydrous systems. The phase transition boundary between Brg and PPv shifts to higher or lower pressures when the hydrogen atom substitutes in the Mg or Si sites in the lattice, respectively. The existence of volatiles such as hydrogen may account for the strong lateral chemical heterogeneity in lowermost mantle.

1. Introduction

Seismic investigations have shown that there is a seismic discontinuity region, or called the D″ layer, above the CMB. Geophysical and geodynamic researches in the D″ layer have been kept on after it was discovered. The D″ layer contains strong seismic anisotropy and is characterized by an anticorrelation between the shear and bulk wave velocities, seismic discontinuity, large low-shear-velocity provinces (LLSVPs) with −1 to −5% S-wave velocity anomaly (Ford et al., 2006; He and Wen, 2012), and a strong topography with laterally varying thickness from 0 to over 300 km (Cobden et al., 2015; Garnero and McNamara, 2008; Lay and Garnero, 2011). These features have commonly been explained by chemical heterogeneity (Wicks et al., 2010), partial melting (Fiquet et al., 2010), preferred orientations (Murakami et al., 2004), and mineral phase transitions (Murakami et al., 2004; Oganov and Ono, 2004). The discovery of the phase transition from Bridgmanite (Brg) to post-Perovskite (PPv) at the pressure–temperature condition corresponding to the top of the D″ layer has been invoked to explain those of the anomalous features within the D″ region (Nowacki et al., 2010; Oganov and Ono, 2004; Tsuchiya et al., 2004).

$MgSiO_3$ Brg to PPv phase transformation was reported at the conditions of 125–127 GPa and 2500–3000 K, corresponding to about 2740 km depth (Murakami et al., 2004; Oganov and Ono, 2004; Tsuchiya et al., 2004). However, recent experimental and theoretical studies have shown that the real phase transition between Brg and PPv in lowermost mantle is much more complicated than that in the pure $MgSiO_3$ system (Dorfman et al., 2013). The presence of Al and Fe can affect the transition thickness and depth of transition boundary between Brg and PPv. Most of the experimental and theoretical studies indicate the addition of Al will stabilize Brg at higher pressure region relative to PPv (Tateno et al., 2005; Zhang and Oganov, 2006a). However, the effect of Fe has been controversial. Some experimental and theoretical studies demonstrated that the presence of Fe could lower the phase transition pressure (Mao et al., 2004; Zhang and Oganov, 2006b), yet other groups suggested that Fe can stabilize Brg relative to PPv in lower mantle (Murakami et al., 2005).

The effects of major element impurities in the phase transition have been studied for a long time. Recently, geochemical evidence suggests that an isolated primordial volatile reservoir should exist in the lowermost mantle to explain isotope features (Gonnermann and Mukhopadhyay, 2007; Hallis et al., 2015). The effect of these volatile such as water on the Brg-PPv phase transition and physical properties has not been deeply explored. Water incorporates into the crystal lattice as hydrogen defect through charge-coupled substitution mechanism, which is formed by Si, Mg vacancy de-

* Corresponding author.
E-mail address: zhangfeiwu@vip.gyig.ac.cn (F. Zhang).

https://doi.org/10.1016/j.epsl.2019.115753
0012-821X/

fect or coupled substitution of other cations (Keppler and Bolfan-Casanova, 2006; Wright, 2006). The transition zone has a large water storage capacity, where Olivine polymorphs, Wadsleyite, and Ringwoodite can incorporate 1–2 wt.%H_2O into mineral structures (Inoue et al., 2010). Recent evidence from deep diamond, which included in Ringwoodite, indicates that that water content of transition zone is up to 1 wt.% (Pearson et al., 2014). The water storage capacity of the lower mantle remains controversial due to the inconsistent estimate of the water content of lower mantle mineral. Previous experimental evidence suggests that the water storage capacity of Bridgmanite and Ferropericlase would be no more than $\sim$ 20 ppm (Bolfan-Casanova et al., 2003; Panero et al., 2015), some synthesis experiments, however, indicate more wide contents ranging from 50 ppm to 0.4 wt.% (Litasov et al., 2003; Murakami et al., 2002). Recently, Hernández et al. (2013) used the first-principles method to calculate the hydrogen partition between Ringwoodite, Ferropericlase, and Bridgmanite, which concludes that Bridgmanite may contain up to 1000 ppm water or even more. Townsend et al. (2016) argued that significant water could be hosted in Al-bearing post-Perovskite in lowermost mantle.

In this study, we perform first-principles calculations to investigate in details the hydrogen incorporation mechanisms and the energetic stabilities of several systems, i.e. (Al, Fe)-free, Al-bearing, Fe-bearing Bridgmanite and post-Perovskite systems. We have also calculated the elastic constants of hydrous Brg and PPv in order to determine the hydration effect on the elastic properties and elastic wave velocities. The density functional perturbation theory is employed to calculate the quasi-harmonic free energies of hydration mechanisms, the P–T phase diagram of hydration system is, therefore, re-plotted.

2. Computational details

2.1. First principles calculations

Our simulations were performed using the VASP code (Kresse and Furthmuller, 1996), an efficient program that implements density functional theory (DFT) using the all-electron PAW method (Kresse and Joubert, 1999). In all calculations, the exchange-correlation energy was computed using the PBE form of Generalized Gradient Approximation (GGA) (Perdew et al., 1996), and we used $1S^2$ core (radius 1.52 a.u.) for O, $1S^22S^2$ core (radius 2 a.u.) for Mg, $1s^22s^22p^6$ core (radius 1.9 a.u.) for Si, $1s^22s^22p^6$ core (radius 1.9 a.u.) for Al, $1s^22s^22p^63s^23p^6$ core (radius 2.3 a.u.) for Fe and ultrasoft pseudopotential for H. We used 2X2X1 and 4X1X1 supercells with 80-atom for Bridgmanite and post-Perovskite, respectively. The plane-wave cut-off of 600 eV was set for representing the wave functions. The K-space mesh was generated by the 3X3X4 Monkhorst–Pack grid (Monkhorst and Pack, 1976) for the 80-atom supercells. All incorporation structures were relaxed at static conditions (0 K) and pressure range of 70–130 GPa, with an interval of 10 GPa. Structural optimization was performed by the conjugate-gradients method until the total energy changes were less than 10^{-6} eV. A force convergence criterion was set to 0.01 eV/Å. The force constant matrixes were calculated by using density functional perturbation theory (DFPT) (Gonze and Lee, 1997), and the phonon dispersion curve obtained by using PONONPY code (Togo et al., 2010) with 2X2X2 q-point mesh.

To be noticed, in this study, we mainly compare the energy differences between different hydrous lower mantle minerals. The energy contribution of the +U term will be canceled when we calculate the energy difference between iron-bearing systems. Therefore, we are only discussing the results produced from PBE without adding the empirical Hubbard parameter U correction term to the strongly correlated electrons in Fe bearing systems.

2.2. Quasi-harmonic approximation (QHA) calculation

We performed the QHA calculations to obtain the Gibbs free-energy (G) at high pressures and temperatures, which can be expressed as a minimization problem in the equilibrium volume (V) at the certain pressure (P) and temperature (T) conditions (Togo et al., 2010):

$$G(P,T) = \min_V \left[U_{\text{static}}(V) + F_{\text{phonon}}(T;V) + PV \right] \tag{1}$$

where U_{static} is the total energy of the static lattice at volume V. Under the QHA framework the phonon vibrational contribution to the Helmholtz free energy $F_{\text{phonon}}(P;V)$ can be written as:

$$F_{\text{phonon}}(T;V) = \sum_{s,q} \frac{1}{2}\hbar\omega_s(q;V) + k_BT \sum_{s,q} \ln\left(1 - \exp\left(-\frac{\hbar\omega_s(q;V)}{k_BT}\right)\right) \tag{2}$$

where q and s are the wave vector and band index, respectively, and $\omega_s(q;V)$ is the frequency of the phonon at q and volume V. k_BT and $\hbar$ are the Boltzmann constant and reduced Planck constant, respectively.

3. Results and discussion

3.1. Substitution mechanism of hydrogen

Generally, the incorporation of hydrogen into nominally anhydrous minerals is related to the protonation of O atoms that controlled by charge balance in the mineral structure and is achieved by Si, Mg vacancy substitution or coupled substitution with other cations. Bridgmanite and post-Perovskite both are orthorhombic and have the similar feature of crystal chemistry with Si in sixfold coordination, Mg in eightfold coordination, and two distinct oxygen sites, i.e., O_1 and O_2. In order to investigate the stability of potential hydrogen defect configuration, and confirm the appropriate hydrogen substitution mechanism, we considered seven hydrogen defects: $V_{Mg}2H$ defect ($V''_{Mg} + 2OH^{\bullet}$) (1.140 wt.%H_2O), $V_{Si}4H$ defect ($V''''_{Si} + 4OH^{\bullet}$) (2.284 wt.%$H_2O$), $Al_{Si}H$ defect ($Al'_{Si} + OH^{\bullet}$) (0.563 wt.%H_2O), $Al_{Mg}H$ defect ($V''_{Mg} + Al^{\bullet}_{Mg} + OH^{\bullet}$) (0.570 wt.%$H_2O$), $Fe^{3+}{}_{Si}H$ defect ($Fe'_{Si} + OH^{\bullet}$) (0.552 wt.%H_2O), $Fe^{3+}{}_{Mg}H$ defect ($V''_{Mg} + Fe^{\bullet}_{Mg} + OH^{\bullet}$) (0.559 wt.%$H_2O$), $Fe^{2+}{}_{Mg}2H$ defect ($V''_{Mg} + Fe^{x}_{Mg} + 2OH^{\bullet}$) (1.118 wt.%$H_2O$); (defects are described using Kröger–Vink defect notation, $\bullet$ and $'$ superscripts represent a positive or negative net charge on the site, respectively). The initial H-atom positions for Mg site were determined according the studies of Townsend et al. (2015, 2016). The initial H-atom positions for Si site were determined by the OH bond along the edge of SiO_6 octahedron. Through calculation of phonon dispersion and enthalpy of all defect configurations at mantle pressure conditions, we have eliminated those structures that have unstable phonon dispersion and relatively high energy. The enthalpy of different configurations for the same hydrogen substitution mechanism is presented in Supplementary material (Table A.1–A.3). The crystal structures which are used for subsequent property calculation are shown in Fig. 1–3. We will divide above seven hydrogen defects into three systems to discuss: (Al, Fe)-free system, Al-bearing system, and Fe-bearing system.

For (Al, Fe)-free system, $V_{Mg}2H$ and $V_{Si}4H$ are comparatively common hydrogen defects in research about aquosity of minerals (Wright, 2006). As illustrated in Fig. 1A and Fig. 1B, in the case of $V_{Mg}2H$ defect in Bridgmanite, we have found a stable structure in which two hydrogen atoms occupy the site of an Mg vacancy

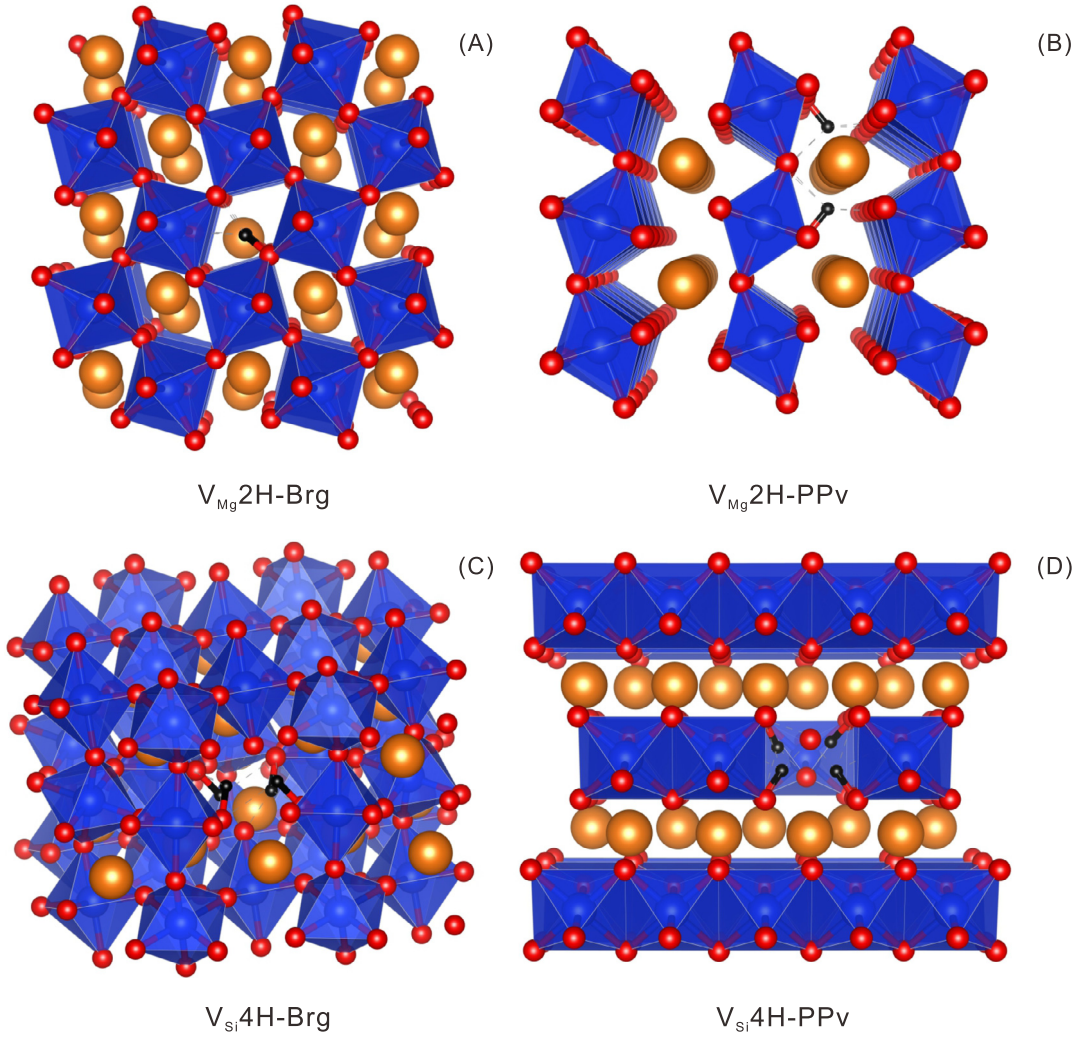

Fig. 1. Crystal structures used in the (Al, Fe)-free system. (A). V_{Mg}2H-Brg crystal structure. (B). V_{Mg}2H-PPv crystal structure. (C). V_{Si}4H-Brg crystal structure. (D). V_{Si}4H-PPv crystal structure. In all structures orange, dark blue, red and black spheres represent magnesium, silicon, oxygen, and hydrogen, respectively. (For interpretation of the colors in the figure(s), the reader is referred to the web version of this article.)

and bond with two O_2 atoms as hydroxyl. Similarly, the structure of V_{Mg}2H defect in post-Perovskite, an Mg vacancy is occupied by two protons, which bond with two O_2 atoms as well. Fig. 1C and Fig. 1D illustrate the structure of V_{Si}4H defect in Bridgmanite and post-Perovskite. The Si vacancy is filled by four hydrogen atoms. Each hydrogen bond with an O_2 atom at SiO_6 octahedron as a hydroxy group, which connects to one of the two unbonded O_1 through hydrogen bond.

In Al-bearing system, the stable structure of Al_{Si}H-Brg and Al_{Si}H-PPv at 120 GPa are illustrated in Fig. 2A and Fig. 2B. In this case, an aluminum atom and a hydrogen atom jointly incorporate into the lattice at the Si site, where the hydrogen occupies an interstitial site and bonds with O_1 atom. Alternatively, in order to evaluate the effect caused by the Al atom that occupies different sites, we have modeled the configuration with the Al atom occupying an Mg vacancy site, (Al_{Mg}H defect) for Brg and PPv. The stable structures of Al_{Mg}H-Brg and Al_{Mg}H-PPv are shown in Fig. 2C and Fig. 2D respectively. The hydrogen atom occupies another nearest Mg vacancy. Note that the hydrogen is bonding with O_1 in Al_{Mg}H-Brg, with O_2 in Al_{Mg}H-PPv.

The presence of Fe has a significant effect on the chemical and physical properties of dry Brg and PPv, such as density, elasticity, and phase transition boundary (Fukui et al., 2016; Muir and Brodholt, 2015; Sun et al., 2018). However, the coupled influence of iron and hydrogen has not been determined yet. Hence, we considered $Fe^{3+}{}_{Si}$H, $Fe^{3+}{}_{Mg}$H, and $Fe^{2+}{}_{Mg}$2H defects to determine this influence. In $Fe^{3+}{}_{Si}$H defect, coupled Fe^{3+} and hydrogen occupy Si site by replacing the Si atom, in which hydrogen atom bonds with O_1, which are shown in Fig. 3A and Fig. 3B. For the $Fe^{3+}{}_{Mg}$H defect in Brg and PPv, the stable structure we have found is that a Fe^{3+} occupies an Mg site via removing an Mg atom, and a hydrogen atom that bonds with O_1, occupies an adjacent Mg vacancy site as illustrated in Fig. 3C and Fig. 3D. $Fe^{2+}{}_{Mg}$2H defect has a stable structure as like with Al_{Mg}H, which is shown in Fig. 3E and Fig. 3F. Fe^{2+} substitutes into the lattice at the Mg site, and two hydrogen atoms occupy another nearest Mg vacancy, bonded with O_2.

The hydrogen bond geometry for all the stable configurations at 120 GPa is presented in Table 1, and at 70 GPa is presented in Supplementary material (Table A.4). In all simulated structures, both $d(O\ldots O)$ and $d(O\ldots H)$ are shortened with pressure increases. This trend is consistent with previous results reported by Blanchard et al. (2009). From the pressure of 70 GPa to 120 GPa, the degree of decrease of $d(O\ldots H)$ in $Fe^{3+}{}_{Mg}$H-Brg is the largest among all studied structures, which is reduced by 0.198 Å (10%). In contrast, the degree of decrease of $d(O\ldots H)$ is the smallest in $Fe^{3+}{}_{Si}$H-Brg, with about 0.034 Å (2.4%). $d(O\ldots O)$ in PPv is generally shorter than that in Brg, therefore the hydrogen bond will be stronger in PPv, which is agreed well with the recent calculations

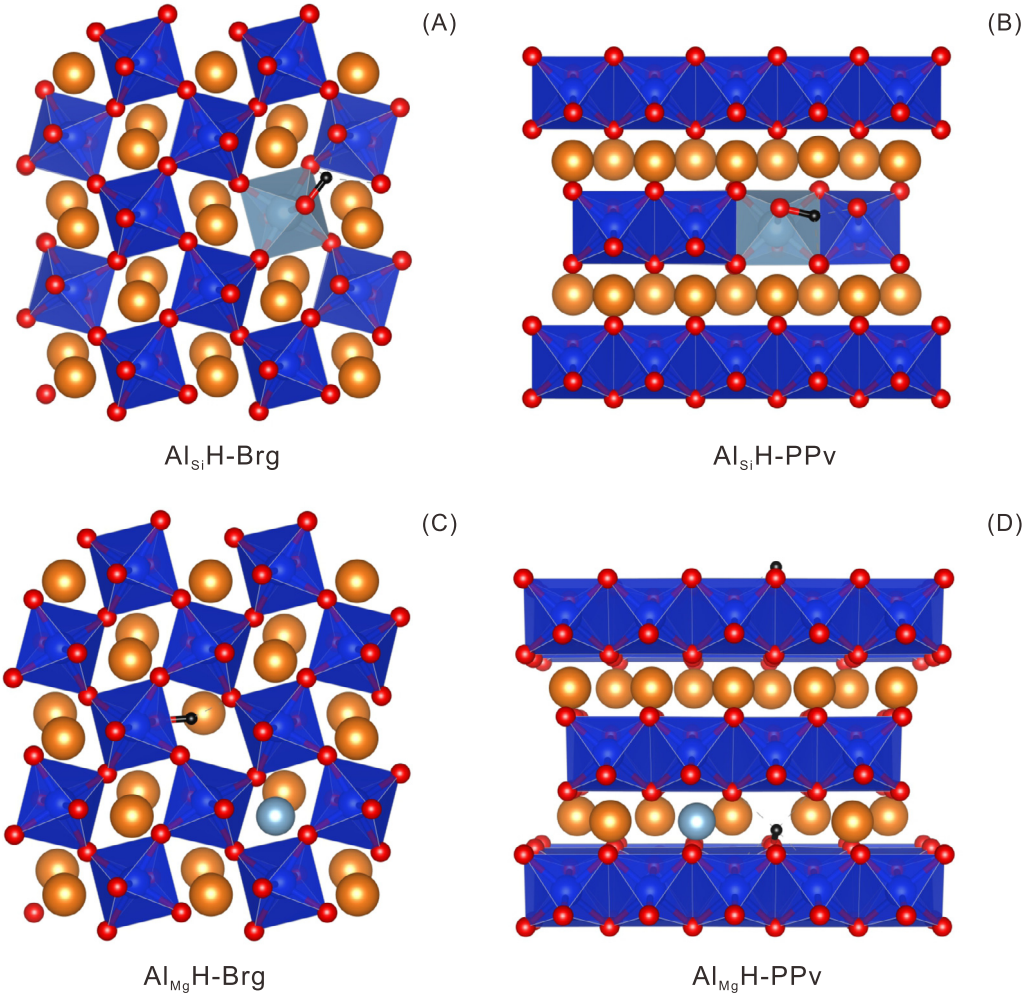

Fig. 2. Crystal structures used in the Al-bearing system. (A). $Al_{Si}H$-Brg crystal structure. (B). $Al_{Si}H$-PPv crystal structure. (C). $Al_{Mg}H$-Brg crystal structure. (D). $Al_{Mg}H$-PPv crystal structure. In all structures orange, dark blue, red, light blue and black spheres represent magnesium, silicon, oxygen, and hydrogen, respectively.

Table 1
Hydrogen-bond geometries at 120 GPa for Brg and PPv-phase used in this study.

	Structure	d(O–H) (Å)	d(O…O) (Å)	d(O…H) (Å)	H-bond angle (°)
(Al, Fe)-free	$V_{Mg}2H$-Brg	0.999	2.399	1.819	113.54
	$V_{Mg}2H$-PPv	0.995	2.305	1.704	114.76
	$V_{Si}4H$-Brg	1.030	2.307	1.288	168.70
	$V_{Si}4H$-PPv	1.063	2.324	1.267	171.68
Al-bearing	$Al_{Si}H$-Brg	1.049	2.371	1.372	156.42
	$Al_{Si}H$-PPv	1.067	2.341	1.325	156.15
	$Al_{Mg}H$-Brg	1.014	2.570	1.767	133.28
	$Al_{Mg}H$-PPv	0.994	2.276	1.683	114.01
Fe-bearing	$Fe^{3+}{}_{Si}H$-Brg	1.039	2.367	1.381	155.71
	$Fe^{3+}{}_{Si}H$-PPv	1.083	2.330	1.297	156.40
	$Fe^{3+}{}_{Mg}H$-Brg	1.013	2.580	1.776	133.56
	$Fe^{3+}{}_{Mg}H$-PPv	1.031	2.285	1.402	139.42
	$Fe^{2+}{}_{Mg}2H$-Brg	0.998	2.405	1.787	116.59
	$Fe^{2+}{}_{Mg}2H$-PPv	0.995	2.302	1.705	114.40

(Townsend et al., 2016). We have also found that the hydrogen bond in Silicon-site related $V_{Si}4H$, $Al_{Si}H$, and $Fe^{3+}{}_{Si}H$ configurations, with the hydrogen bond angle of around 170.19°, 156.29°, and 156.06° respectively, are comparatively more linear than that in Magnesium-site related $V_{Mg}2H$, $Al_{Mg}H$, $Fe^{3+}{}_{Mg}H$, and $Fe^{2+}{}_{Mg}2H$ configurations. The calculated O-H distances in Silicon-site related configurations are relatively longer than that in Magnesium-site related configurations

The hydrogarnet-type substitution, where the Si vacancy is charge-compensated by four protons, usually presences in upper mantle minerals, especially in Ringwoodite (Wright, 2006). However, the number of Si vacancies produced by water is extremely low compared with the Mg vacancies in Bridgmanite at lowermost mantle (Muir and Brodholt, 2018). In our studied model, we have confirmed the Silicon vacancy mechanism ($MgSi_{0.9375}H_{0.25}O_3$) defect is energetically unstable than Magnesium vacancy mechanism ($Mg_{0.9375}SiH_{0.125}O_3$) by 0.11 eV/f.u. and 0.12 eV/f.u. in Bridgmanite and post-Perovskite, respectively.

To evaluate the relative water storage stability in Al-bearing and Fe-bearing systems for both Brg and PPv phase, we have considered following two reactions ($x = 0.0625$):

$$\left[(Mg_{1-2x}Al_x)SiO_3H_x\right]_{Brg/PPv} + 3xMgO \Leftrightarrow \left[Mg(Si_{1-x}Al_x)O_3H_x\right]_{Brg/ppv} + xMgSiO_{3Brg/PPv} \quad (3)$$

$$\left[(Mg_{1-2x}Fe_x)SiO_3H_x\right]_{Brg/PPv} + 3xMgO \Leftrightarrow \left[Mg(Si_{1-x}Fe_x)O_3H_x\right]_{Brg/PPv} + xMgSiO_{3Brg/PPv} \quad (4)$$

the left-hand side of the equations represents $Al_{Mg}H$ and $Fe^{3+}{}_{Mg}H$ defect, and right-hand side is $Al_{Si}H$ and $Fe^{3+}{}_{Si}H$ defect for Al-bearing and Fe-bearing systems, respectively. The calculated reaction enthalpies ΔH as a function of pressure are shown in Fig. 4.

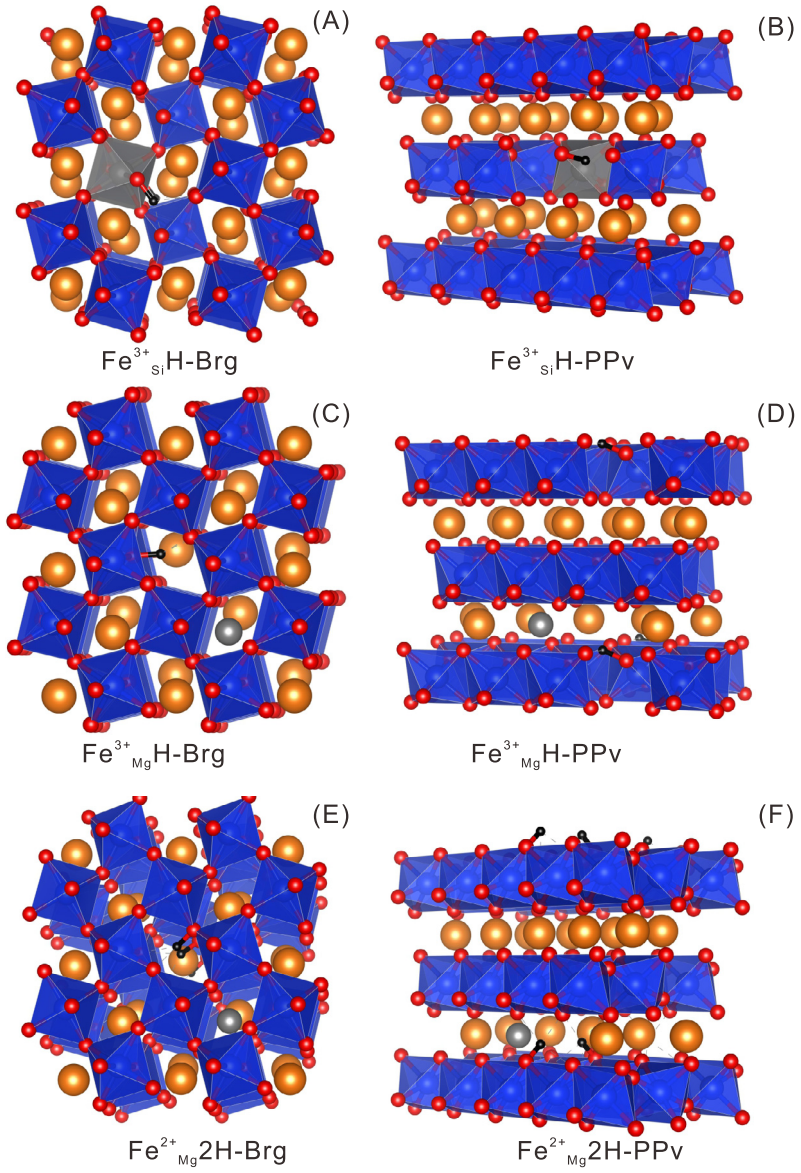

Fig. 3. Crystal structures used in the Fe-bearing system. (A). Fe^{3+}_{Si}H-Brg crystal structure. (B). Fe^{3+}_{Si}H-PPv crystal structure. (C). Fe^{3+}_{Mg}H-Brg crystal structure. (D). Fe^{3+}_{Mg}H-PPv. (E). Fe^{2+}_{Mg}2H-Brg crystal structure. (F). Fe^{2+}_{Mg}2H-PPv crystal structure. In all structures orange, dark blue, red, gray and black spheres represent magnesium, silicon, oxygen, iron, and hydrogen, respectively.

In consistent with recent work (Muir and Brodholt, 2018), we conclude that the Fe^{3+}_{Si}H and Al_{Si}H defects are energetically more favorable than Fe^{3+}_{Mg}H and Al_{Mg}H defects for both Brg and PPV phases under all the lower mantle pressures.

3.2. Elastic properties

In order to investigate the effect of hydrogen on the elastic properties of Brg and PPv, the nine elastic constants of all hydrous structures have been calculated by a stress-strain relation with four different strain magnitudes (± 0.005 and ± 0.01), which are given in Supplementary material (Table A.5 and Table A.6). We found that the elastic constants of pure-Brg and PPV are compared favorably with previous studies (Oganov and Ono, 2004; Zhang et al., 2013). The effects of iron and aluminum on the elasticity properties of dry Brg and PPv have been investigated before (Li et al., 2005; Tsuchiya and Tsuchiya, 2006). Here, we focus on the hydration effect on the elasticity properties in both (Al, Fe)-free and (Al, Fe)-bearing systems.

3.2.1. (Al, Fe)-free system

The existence of hydrogen in V_{Mg}2H and V_{Si}4H defects will mainly reduce the elastic constant of Brg and PPv phase. However, we have also observed some odd variations on elastic constant, for instance, the incorporation of hydrogen increases the C_{66} and C_{23} in both (Al, Fe)-free systems.

The pressure dependence of the isotropic bulk (K) and shear (G) moduli for Brg and PPv phase obtained from the Voigt–Reuss–Hill averaging scheme are shown in Fig. 5A and Fig. 5C, respectively. We find that, K and G of both phases are decreased by hydration. In Brg-phase, K and G of V_{Si}4H defect structure are smaller than those of V_{Mg}2H defect under the studied pressure range, which indicates that the reduced degree of K and G will be affected by water content. However, in PPv-phase, the G moduli of V_{Mg}2H and V_{Si}4H defect structures are very similar throughout most of the pressure ranger of the lower mantle.

The isotropic averaged P-wave (V_P), S-wave (V_S) and bulk sound velocities (V_Φ) are illustrated in Fig. 5B and Fig. 5D. At 120 GPa, the presence of hydrogen decreases the V_P and V_S in

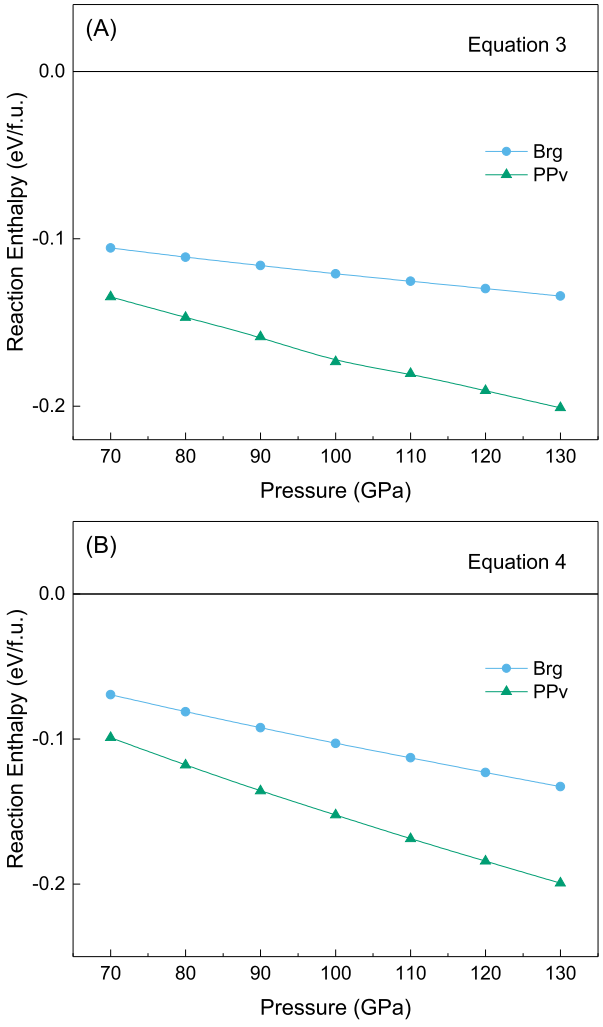

Fig. 4. The reaction enthalpy for Al-bearing system (A) and Fe-bearing system (B) as a function of pressure. The MgO structure is optimized at the pressures of 70–130 GPa. Blue: Brg-phase. Green: PPv-phase.

both Brg and PPv phases. In Brg-phase, V_{Si}4H defect structure's V_P and V_S are smaller than those of V_{Mg}2H defect structure at the low-pressure area (70–100 GPa). This difference is diminished at the high-pressure area over 100 GPa. However, the V_P and V_S of these two defects (V_{Mg}2H and V_{Si}4H) are very comparable at entire pressure range in PPv-phase. The bulk sound velocity is remarkably insensitive to the incorporation of hydrogen, especially in the PPv-phase, which consist with previous study (Townsend et al., 2015).

The single crystal elastic wave velocities were obtained by solving the Christoffel equation:

$$\det\left|C_{ijkl}n_k n_l - \rho V^2 \delta_{ij}\right| = 0 \tag{5}$$

where C_{ijkl}, n, ρ, V and δ_{ij} are the elastic tensor, propagation direction, density, wave velocity, and Kronecker delta, respectively.

The single crystal elastic wave velocities of Brg-phase (top) and PPv-phase (bottom) as the function of propagation directions at the pressure of 120 GPa are shown in Fig. 6. The presence of hydrogen does not noticeably change the maximum or minimum velocity propagation directions for both phases. However, the variation of single crystal wave velocities are still affected by incorporation of hydrogen, and the S wave velocities are more sensitive to hydration compared with P wave. Fig. 6A indicates that, at 120 GPa, the V_{Mg}2H-Brg's V_{SH} (horizontally polarized) which along [010] direction is slightly faster than pure-Brg, but V_{SH} of V_{Si}4H-Brg is slower than pure-Brg along the same direction. Besides, V_{SV} of V_{Mg}2H-Brg and V_{Si}4H-Brg are slower than pure-Brg along all directions, especially along [001] and [110] for V_{Mg}2H-Brg. In PPv-phase (Fig. 6B), we observe certain interesting variations of V_S that along some specific propagation direction, for instance, the V_{SH} of V_{Si}4H-PPv is slightly greater than pure-PPv's along [100], [101], [011] and [010] directions, and the V_{SH} of V_{Mg}2H-PPv, whereas, is less than pure-PPv along identical directions. This could attribute to the hydrogen occupied different vacancy in the structure.

3.2.2. Al-bearing system

Tsuchiya and Tsuchiya (2006) have demonstrated that Al and Fe impurity reduce the shear elastic moduli (C_{44}, C_{55}, C_{66}) of Brg and PPv observably. Here, we estimate the coupled effect caused by Al and hydrogen on the elasticity property. For Brg-phase, $Al_{Si}H$ defect structure that an Al and hydrogen jointly occupied a Si vacancy decreases C_{11}, C_{33}, C_{12}, C_{44}, and C_{55} mightily, yet increase C_{66} slightly. $Al_{Mg}H$ defect structure, with coupled an Al and two hydrogens at two Mg vacancies, has an opposite variation on C_{11} compared with $Al_{Si}H$-Brg. For PPv-phase, $Al_{Si}H$ defect reduces the longitudinal moduli (C_{11}, C_{22}, and C_{33}) and shear moduli (C_{44}, C_{55}, and C_{66}). However, in $Al_{Mg}H$-PPv, the C_{11}, C_{33}, C_{23}, and shear moduli are decreased with hydration.

Fig. 5A and 5C present the aggregate bulk and shear moduli of $Al_{Si}H$-Brg/PPv and $Al_{Mg}H$-Brg/PPv calculated from the Voigt–Reuss–Hill average. Compared to pure-Brg phase, the incorporation of aluminum and hydrogen reduces the K and G of Brg-phase under the lower mantle pressures. At 120 GPa, the bulk moduli of $Al_{Si}H$-Brg and $Al_{Mg}H$-Brg are $\sim$ 10.7 GPa per wt.%H_2O and $\sim$ 3.5 GPa per wt.%H_2O smaller than pure-Brg; the shear moduli are $\sim$ 10.7 GPa per wt.%H_2O and $\sim$ 8.8 GPa per wt.%H_2O smaller, respectively. For PPv-phase, $Al_{Si}H$ and $Al_{Mg}H$ decrease the K and G of PPv as well, and the effect of hydration on shear moduli is more sensitive than Brg-phase. The bulk moduli of $Al_{Si}H$-PPv and $Al_{Mg}H$-PPv are smaller than pure-PPv by $\sim$ 10.7 GPa per wt.%H_2O and $\sim$ 5.3 GPa per wt.%H_2O, and the shear moduli are $\sim$ 16.0 GPa per wt.%H_2O and $\sim$ 19.3 GPa per wt.%H_2O smaller than pure-PPv.

The calculated P-wave (V_P), S-wave (V_S) and bulk sound (V_Φ) velocities of Al-bearing system are demonstrated in Fig. 5B for Brg-phase and Fig. 5D for PPv-phase, respectively. The isotropic velocities of $Al_{Si}H$-Brg are smaller than those of pure-Brg at 120 GPa by $\sim$ 0.9% per wt.%H_2O for P-wave (V_P) and $\sim$ 1.2% per wt.%H_2O for S-wave (V_S). $Al_{Mg}H$-Brg's V_P and V_S are $\sim$ 0.5% per wt.%H_2O and $\sim$ 1.2% per wt.%H_2O lower than those of pure-Brg. In PPv-phase, velocities of $Al_{Si}H$-PPv at 120 GPa are smaller than those of pure-PPv by $\sim$ 1.1% per wt.%H_2O for V_P and $\sim$ 2.0% per wt.%H_2O for V_S. $Al_{Mg}H$-PPv have $\sim$ 2.6% per wt.%H_2O and $\sim$ 2.5% per wt.%H_2O smaller V_P and V_S than pure-PPv. We note that the bulk sound velocities (V_Φ) are remarkably insensitive to the presence of hydrogen with a variation that less than $\sim$ 0.3%.

The effect of coupled Al and H on the single crystal elastic wave velocities calculated from Eq. (5) at 120 GPa are shown in Fig. 6. In Brg-phase (Fig. 6C), $Al_{Si}H$ defect does not change the propagation directions of fastest and slowest wave velocity. The fastest and slowest propagation directions for V_P is along [010] and [100], respectively. The fastest and slowest propagation directions for V_S is along [001] and [110], respectively. However, for $Al_{Mg}H$-Brg, the slowest direction of V_S changes to [100], due to the small C_{55} of $Al_{Mg}H$-Brg. In PPv-phase (Fig. 6D), $Al_{Mg}H$-PPv has a propagation direction dependence of wave velocities which is identical with pure-PPv. Here its V_P is fastest and slowest in the [100] and [010] directions respectively, as determined by ordering $C_{11} > C_{33} > C_{22}$. The fastest V_S propagate along [101] direction, and the slowest propagation direction is in [100] and [001] respectively, consistent with the small C_{55}. This result is consistent with the observation by Tsuchiya and Tsuchiya (2006). For $Al_{Si}H$-PPv, the V_P is still

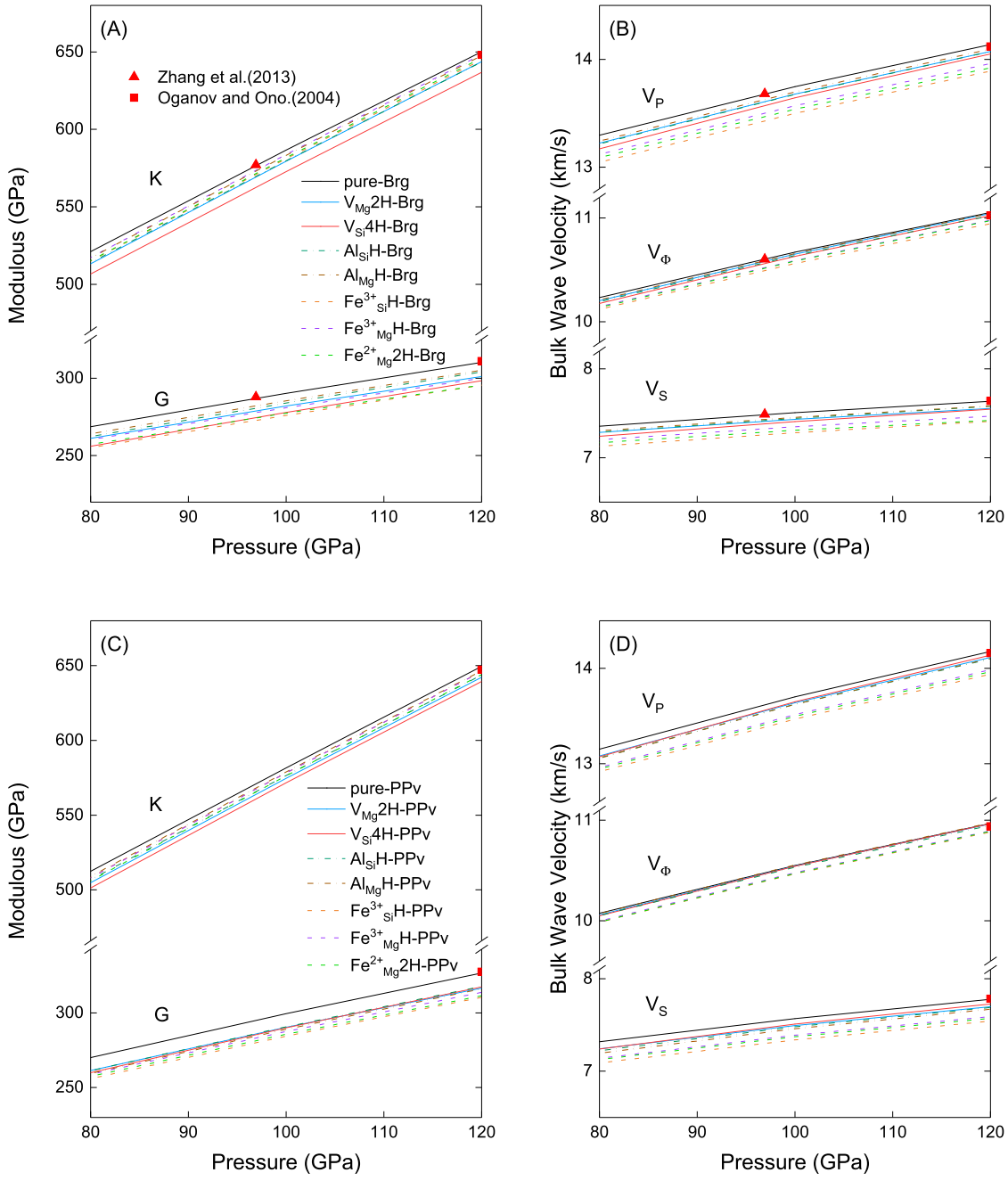

Fig. 5. Bulk elastic properties of pure-Brg/PPv (black), V_{Mg}2H-Brg/PPv (blue), V_{Si}4H-Brg/PPv (red), Al_{Si}H-Brg/PPv (dark green), Al_{Mg}H-Brg/PPv (brown), $Fe^{3+}{}_{Si}$H-Brg/PPv (orange), $Fe^{3+}{}_{Mg}$H-Brg/PPv (purple) and $Fe^{2+}{}_{Mg}$2H-Brg/PPv (green). Voigt–Reuss–Hill averaged bulk moduli (K) and shear moduli (G) for Brg-phase (A) and PPv-phase (C) as a function of pressure. Isotropic bulk wave velocities for Brg-phase (B) and PPv-phase (D) as a function of pressure.

fastest along [100] and slowest along [010] direction. The fastest direction of V_S remain unchanged, yet one of the slowest V_S propagation directions changes to [010] which correspond to small C_{44}.

3.2.3. Fe-bearing system

We have investigated the coupled hydrogen and iron effect on elasticity properties of Brg and PPv, and the results are summarized in Supplementary material (Table A.5 and Table A.6). Various iron valence states have been considered. In Brg-phase, we find that the joint substitution of a Fe^{3+} and a hydrogen for one Si vacancy ($Fe^{3+}{}_{Si}$H-Brg) reduces the longitudinal moduli (C_{11}, C_{22}, and C_{33}) and shear moduli (C_{44}, C_{55}, and C_{66}), and increases the off-diagonal moduli (C_{12}, C_{13}, and C_{23}). The similar trend on elastic moduli can be observed in $Fe^{3+}{}_{Mg}$H-Brg as well except that the C_{11} and C_{66} are relatively unchanged. For $Fe^{2+}{}_{Mg}$2H-Brg, a Fe^{2+} and two hydrogen atoms occupy two Mg vacancies, reduces the C_{11}, C_{22} and shear moduli (C_{44}, C_{55}, and C_{66}), and leaving the C_{33}, C_{13} relatively unchanged. For PPv-phase, we find a common variation trend in $Fe^{3+}{}_{Si}$H-PPv, $Fe^{3+}{}_{Mg}$H-PPv, and $Fe^{2+}{}_{Mg}$2H-PPv, which is decreases on the longitudinal moduli (C_{11}, C_{22}, and C_{33}) and shear moduli (C_{44}, C_{55}, and C_{66}), and increases on the C_{12}, C_{13}. The C_{23} of $Fe^{3+}{}_{Mg}$H-PPv and $Fe^{2+}{}_{Mg}$2H-PPv are reduced with the incorporation of iron and hydrogen.

Aggregate bulk and shear moduli of Brg and PPv phases are shown in Fig. 5A, 5C and Supplementary material (Table A.5, A.6). Compared to pure-Brg and PPv phase at 120 GPa, the bulk moduli (K) of $Fe^{3+}{}_{Si}$H are ~ 9.1 GPa per wt.%H_2O (Brg) and ~ 7.2 GPa per wt.%H_2O (PPv) smaller, and $Fe^{3+}{}_{Mg}$H have ~ 3.6 GPa per wt.%H_2O (Brg) and ~ 7.2 GPa per wt.%H_2O (PPv) smaller bulk moduli. The

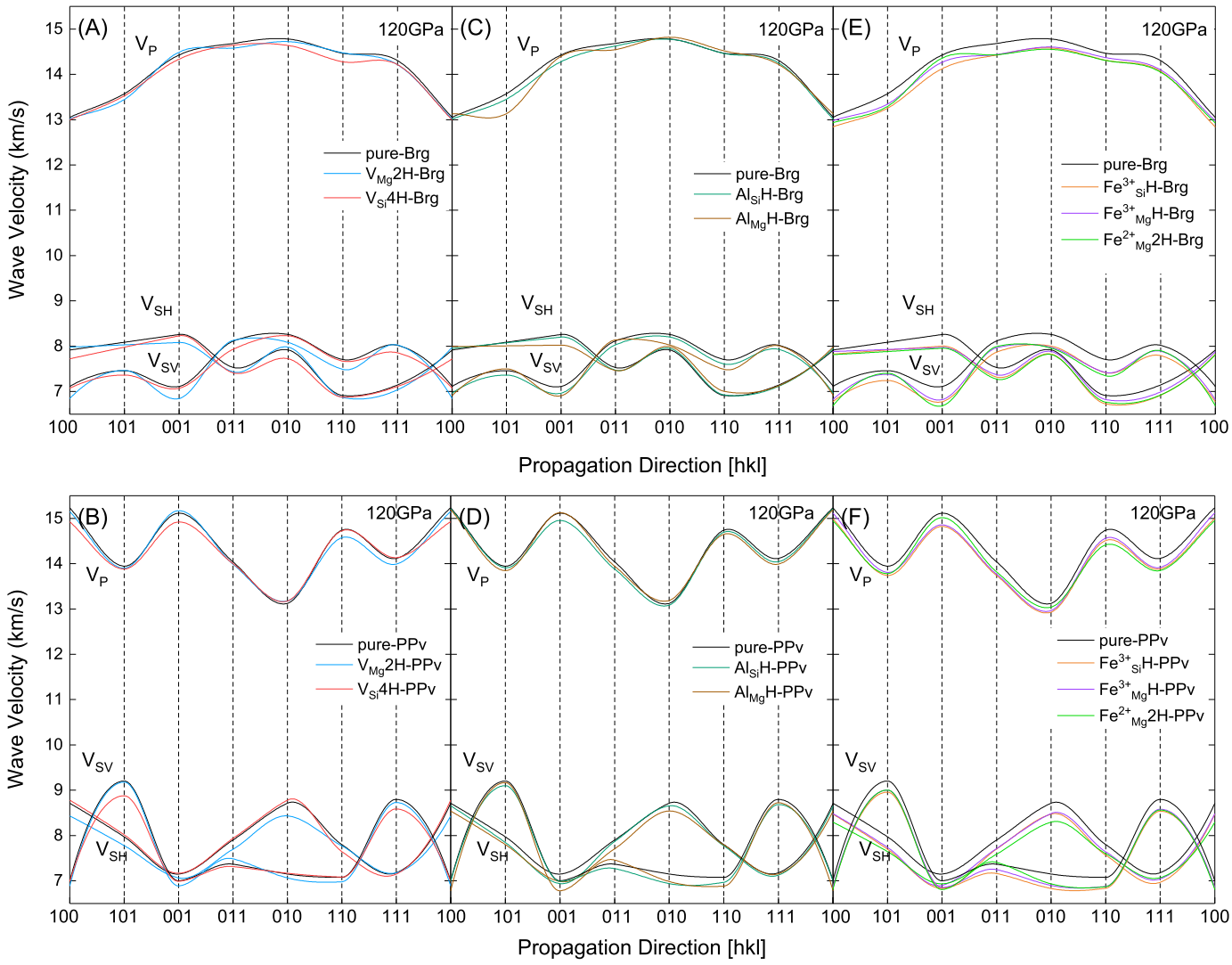

Fig. 6. Variation of single crystal elastic wave velocities of Brg-phase (top) and PPv-phase (bottom) with propagation direction at the pressure of 120 GPa. Black: pure. Blue: V_{Mg}2H. Red: V_{Si}4H. Dark green: Al_{Si}H. Brown: Al_{Mg}H. Orange: $Fe^{3+}{}_{Si}$H. Purple: $Fe^{3+}{}_{Mg}$H. Green: $Fe^{2+}{}_{Mg}$2H.

incorporation of coupled ferrous and hydrogen reduces the bulk moduli as well, with ~ 3.6 GPa per wt.%H_2O for Brg and ~ 5.4 GPa per wt.%H_2O for PPv. The bulk moduli are less sensitive to the substitution of iron and hydrogen. In contrast, the effects of iron and hydrogen on the shear moduli (G) are significant. At 120 GPa, $Fe^{3+}{}_{Si}$H have ~ 27.2 GPa per wt.%H_2O (Brg) and ~ 30.8 GPa per wt.%H_2O (PPv) smaller G, $Fe^{3+}{}_{Mg}$H have ~ 17.9 GPa per wt.%H_2O (Brg) and ~ 23.3 GPa per wt.%H_2O (PPv) smaller G. Shear moduli of $Fe^{2+}{}_{Mg}$2H are ~ 13.4 GPa per wt.%H_2O (Brg) and ~ 14.3 GPa per wt.%H_2O (PPv) smaller. These findings indicate that the presence of iron (ferric or ferrous) and hydrogen strongly reduce the shear moduli G of the lower mantle minerals, especially for PPv-phase.

The isotropic averaged P-wave (V_P), S-wave (V_S) and bulk sound (V_Φ) velocities of Fe-bearing system are plotted in Fig. 5B and Fig. 5D, respectively. For Brg-phase, V_P in $Fe^{3+}{}_{Si}$H, $Fe^{3+}{}_{Mg}$H and $Fe^{2+}{}_{Mg}$2H systems are ~ 3.1% per wt.%H_2O, ~ 2.1% per wt.%H_2O and ~ 1.3% per wt.%H_2O smaller than that of pure dry Brg, respectively and V_S are smaller than those of pure-Brg at 120 GPa by ~ 5.4% per wt.%H_2O, ~ 3.9% per wt.%H_2O, and ~ 2.5% per wt.%H_2O. In PPv-phase the V_P are smaller than those of pure dry PPv at 120 GPa by ~ 3.1% per wt.%H_2O, ~ 2.5% per wt.%H_2O and ~ 1.3% per wt.%H_2O for $Fe^{3+}{}_{Si}$H, $Fe^{3+}{}_{Mg}$H and $Fe^{2+}{}_{Mg}$2H, which have ~ 5.4% per wt.%H_2O, ~ 4.3% per wt.%H_2O and ~ 2.4% per wt.%H_2O smaller V_S than pure-PPv, respectively. Here the bulk sound velocities (V_Φ) for both Brg and PPv-phases are remarkably insensitive to the incorporation of hydrogen and iron.

We determined the single crystal elastic wave velocities of Fe-bearing system by solving the Eq. (5) at 120 GPa, which are plotted in Fig. 6. For Brg-phase (Fig. 6E). The presence of Fe^{3+} and hydrogen does not change the fastest and slowest V_P direction in the $Fe^{3+}{}_{Si}$H defect structure, which are along [010] and [100], respectively. The V_S fastest, [001] and [010], and the slowest, [110], directions are also unchanged. However, for $Fe^{3+}{}_{Mg}$H and $Fe^{2+}{}_{Mg}$2H, the slowest direction of V_S changes to [100] from [110]. For PPv-phase (Fig. 6F), $Fe^{3+}{}_{Si}$H, $Fe^{3+}{}_{Mg}$H, and $Fe^{2+}{}_{Mg}$2H defects do not change the fastest and slowest V_P direction. We can see that their V_P are fastest and slowest in the [100] and [001] directions respectively, which correspond to $C_{11} > C_{33} > C_{22}$. The fastest V_S directions of $Fe^{3+}{}_{Si}$H, $Fe^{3+}{}_{Mg}$H, and $Fe^{2+}{}_{Mg}$2H defect structures are still unchanged, which are along [101] direction. However, one of the slowest V_S directions for $Fe^{3+}{}_{Si}$H is altered from [100] to [010], which caused by a small C_{44}.

3.3. Equations of state and phase transition

We have fitted the isothermal 3rd-order Birch–Murnaghan equations of state for all hydrogen defect configurations at the

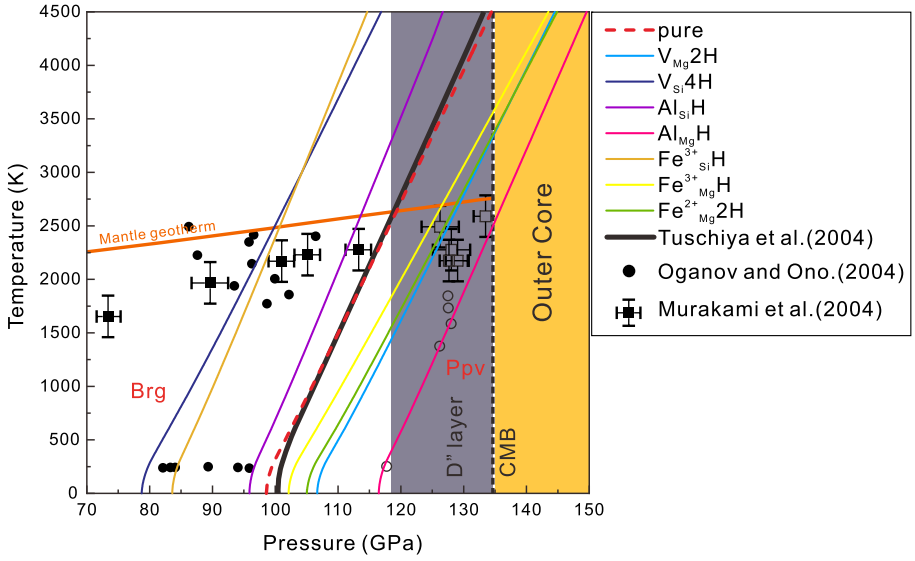

Fig. 7. Calculated phase boundary between Brg and PPv in various hydrogen defects. Red dashed line: pure. Light blue: $V_{Mg}2H$. Dark blue: $V_{Si}4H$. Purple: $Al_{Si}H$. Pink: $Al_{Mg}H$. Dark yellow: $Fe^{3+}{}_{Si}H$. Yellow: $Fe^{3+}{}_{Mg}H$. Green: $Fe^{2+}{}_{Mg}2H$. Shaded gray area: D″ layer. The vertical black dashed line represents the core mantle boundary (CMB). The bold black line represents the phase boundary from the previous study (Tsuchiya et al., 2004). Filled and open points represent an experimental observation of Brg and PPv, respectively (Murakami et al., 2004; Oganov and Ono, 2004). The orange line represents normal mantle geotherm (Brown and Shankland, 1981).

Table 2
Calculated equation of state (EOS) parameters of all hydrous structures for Bridgmanite and post-Perovskite. K_0, V_0 and K_0' were obtained by fitting 3rd-order Birch–Murnaghan equation of state.

	Structure	K_0 (GPa)	V_0 (Å^3)	K_0'	Structure	K_0 (GPa)	V_0 (Å^3)	K_0'
	pure-Brg	241	668.17	3.83	pure-PPv	218	666.77	4.02
(Al, Fe)-free	$V_{Mg}2H$-Brg	228	670.13	3.88	$V_{Mg}2H$-PPv	202	671.61	4.16
	$V_{Si}4H$-Brg	223	677.12	3.87	$V_{Si}4H$-PPv	198	676.77	4.16
Al-bearing	$Al_{Si}H$-Brg	232	675.71	3.84	$Al_{Si}H$-PPv	206	675.91	4.13
	$Al_{Mg}H$-Brg	233	664.80	3.87	$Al_{Mg}H$-PPv	208	665.88	4.12
Fe-bearing	$Fe^{3+}{}_{Si}H$-Brg	233	676.41	3.84	$Fe^{3+}{}_{Si}H$-PPv	209	675.51	4.09
	$Fe^{3+}{}_{Mg}H$-Brg	232	667.89	3.88	$Fe^{3+}{}_{Mg}H$-PPv	205	670.19	4.15
	$Fe^{2+}{}_{Mg}2H$-Brg	231	670.98	3.87	$Fe^{2+}{}_{Mg}2H$-PPv	204	672.77	4.14

ground state of 0 K. The EOS parameters of each configuration are listed in Table 2. For all hydrogen defect configurations the incorporation of hydrogen lowers the zero pressure bulk modulus (K_0) especially for PPv-phase, yet the value of K_0' is insensitive to the presence of hydrogen. which is similar to the transition zone minerals such as Wadsleyite and Ringwoodite (Chang et al., 2015; Wang et al., 2019a). We have also found that, for (Al, Fe)-free and Fe-bearing systems, the incorporation of hydrogen increase their zero-pressure volume (V_0), however, for $Al_{Mg}H$ defect structure of Al-bearing system, its V_0 is slightly reduced by hydration.

We calculated the phase transition boundary for all configurations which include pure system and hydrous system by the quasi-harmonic free energy calculations, which is illustrated in Fig. 7. For pure-Brg and pure-PPv phase, we obtain a positive Clapeyron slop with 8.1 MPa/K, which consistent with previous experimental and computational results (Oganov and Ono, 2004; Ohta et al., 2008). The Clapeyron slope of the hydrous system that covers both (Al, Fe)-free, Al-bearing and Fe-bearing are calculated, and the results are listed in Supplementary material (Table A.7).

It's concluded that when the hydrogen occupies Mg vacancy site, the phase transition boundary between Brg and PPv will be pushed to higher pressure, however the Brg-PPv boundary will be reduced to lower pressure when the hydrogen atom substitutes into Si vacancy site.

4. Discussion

4.1. The implications of hydrogen to LLSVPs

The cause of LLSVPs is always under debate. LLSVPs were first considered as the result of thermal heterogeneity or superplumes. However, several seismological observations including the anti-correlation between shear wave and bulk sound velocity anomalies, and the negative-correlation between density and seismic velocity anomalies (Trampert et al., 2004), indicated that the purely thermal effects are insufficient to explain the LLSVPs. It is thus invoked to explain the LLSVPs that compositional heterogeneity due to the enrichment in iron and silicate (Deschamps et al., 2012) and the primordial metallic melt trapped in the deep mantle (Zhang et al., 2016). Recently, the chemical heterogeneity in lower mantle minerals caused by substitution of trivalent cation has been reported to explain the origin of the LLSVPs (Fukui et al., 2016). We calculate the contrast of S-wave velocity (dV_S) and P-wave velocity (dV_P) for hydrogen incorporation system and dry system respectively and use the results to match the S-wave velocity anomaly in LLSVPs (Fig. 8), the result of P-wave anomaly is presented in Supplementary material (Fig. A.1). Fig. 8 shows dry Al-bearing and 0.563–0.570 wt.%H_2O hydrous Al-bearing system reduces the V_S by ~ 0.3% and ~ 0.9%, respectively, dry Fe-bearing and 0.552–1.118 wt.%H_2O hydrous Fe-bearing system reduces the V_S by ~ 1.7% and ~ 2.7%, respectively. (Al, Fe)-free system re-

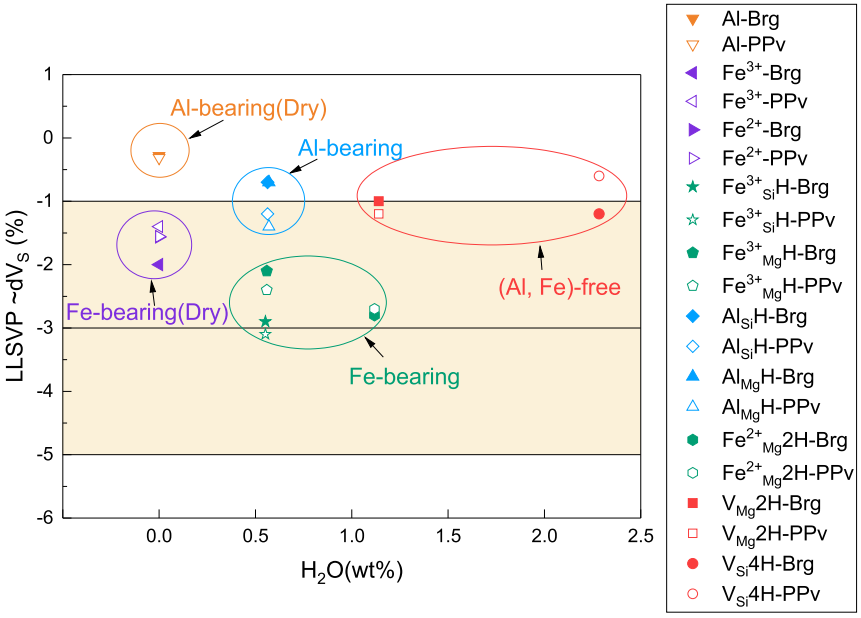

Fig. 8. The calculated S-wave velocity contrasts caused by incorporation of Al (6.25 mol%), Fe (6.25 mol%) and water. The faint yellow horizontal bar in the middle is the range of S-wave velocity anomaly in LLSVPs from seismological observation. Filled and open marks represent Brg-phase and PPv-phase, respectively.

duces the V_S by $\sim 1\%$, which is similar to the Al-bearing system. Our results suggest that, in (Al, Fe)-free system, the reduction of V_S that caused by incorporation of hydrogen and could not match well with the V_S anomaly of LLSVPs. In the 6.25 mol% Al-bearing systems, no matter it's dry or hydrated, its anomalies of V_S are too small to achieve the degree of dV_S in LLSVPs. In both the dry and the hydrous 6.25 mol% Fe-bearing systems, their dV_S are located in the range of values from seismic observations. Particularly, the coupled hydrous and Fe bearing system has a stronger reduction of S-wave velocity than those of dry Fe-bearing system. We also noted that in 0.552 wt.%H_2O hydrous Fe-bearing system, $Fe^{3+}{}_{Si}H$-Brg and $Fe^{3+}{}_{Si}H$-PPv reduce the V_S by $\sim 2.9\%$ and $\sim 3.1\%$ respectively, which are very close to the average value of V_S anomaly in LLSVPs. Our simulations above indicate that the regions depleted in Fe and Al or only Al-enriched in the lowermost mantle might lack clear seismic signature of LLSVPs. The presence of Fe and hydrogen, via the $Fe^{3+}{}_{Si}H$ configuration, would make a significant V_S anomaly in lowermost mantle. Literature estimates the density anomaly of LLSVPs is $\sim 1\%$ positive (Ishii and Tromp, 1999). We have estimated the densities of hydrous Fe-bearing system. The densities are ~ 0.82–1.15% and $\sim 0.6\%$–1.04% heavier than the pure Bridgmanite and post-Perovskite, respectively. Our calculations are in agreement with the studies by Ishii and Tromp (2004), Trampert et al. (2004) and Deschamps et al. (2012). Therefore, we conclude that the hydrous Fe-bearing $MgSiO_3$ might be a dominant component in LLSVPs, and the origin of V_S anomaly in LLSVPs may be due to the water in the lower mantle.

4.2. The implications of hydrogen to the variable topography of D″ layer

High pressure and temperature experimental and theoretical studies have suggested that the phase transition boundary between Brg and PPv would be affected strongly by the composition of mineral (Dorfman et al., 2013; Ohta et al., 2008). Both experimental and theoretical studies have demonstrated the incorporation of Al and Fe could affects the phase transition and coexistence domains between Bridgmanite and post-Perovskite, and then effects the seismological anomalies in lower mantle such as D″ discontinuity(Sun et al., 2018; Wang et al., 2019b). We calculate the variations of phase transition pressure which due to the incorporation of hydrogen. Our results show that, in (Al, Fe)-free system, the $V_{Mg}2H$ defect increases the transition pressure by ~ 9.4 GPa and the $V_{Si}4H$ mechanism decreases the transition pressure by ~ 18.2 GPa. The effect on the Brg-PPv phase boundary in $Al_{Si}H$ (decreases by ~ 5.2 GPa), $Fe^{3+}{}_{Si}H$ (decrease by ~ 17.4 GPa) $Al_{Mg}H$ (increases by ~ 16.5 GPa), $Fe^{3+}{}_{Mg}H$ (increases by ~ 6.6 GPa) and $Fe^{2+}{}_{Mg}2H$ (increases by ~ 8.9 GPa) depends on the Al/Fe substitution site in the lattice. The shift of the Brg-PPv transition pressure due to different incorporation of hydrogen can be represented by the following partial derivative: $\frac{\partial P_{tr}}{\partial x Fe^{3+}{}_{Si}H} = -2.784$ GPa/mol%, $\frac{\partial P_{tr}}{\partial x Al_{Si}H} = -0.832$ GPa/mol%, $\frac{\partial P_{tr}}{\partial x Fe^{2+}{}_{Mg}2H} = 0.712$ GPa/mol%, $\frac{\partial P_{tr}}{\partial x V_{Mg}2H} = 0.754$ GPa/mol% (where P_{tr} is the phase transition pressure and x is the molar concentration of hydrogen in percent). Both previous experimental and theoretical studies have demonstrated that Al is able to enhance the Brg-PPv phase transition pressure (Tateno et al., 2005; Zhang and Oganov, 2006a), and iron would reduce it (Dorfman et al., 2013; Zhang and Oganov, 2006b). Here, an interesting phenomenon can be found in our simulations: whether in (Al, Fe)-free or Al/Fe-bearing system, it will stabilize Bridgmanite to a higher pressure relative to post-Perovskite when the hydrogen incorporates into Mg site. While it will stabilize PPv at a lower pressure when the hydrogen atom incorporates into Si site, In other words, the depth of transition boundary between Brg and PPv may be controlled by the different positions of hydrogen in the mineral lattice, which could explain the laterally varying thickness of D″ layer between 0 and >300 km. Our P–T phase diagram (Fig. 7) suggest that a clear D″ layer boundary in the lowermost mantle may not exist in regions where the hydrogen substitutes into lattice via $Al_{Mg}H$ defect. However, those D″ layer regions, where the $Fe^{3+}{}_{Si}H$ as the dominant defect, should be relatively thicker.

5. Conclusions

We have performed first principles calculations to investigate the incorporation mechanisms of hydrogen in Bridgmanite and post-Perovskite under the lower mantle conditions. In Al-bearing or Fe-bearing system, the hydrogen would more preferentially substitute into the silicon site of the host mineral lattice via $Al_{Si}H$

($Al'_{Si} + OH^{\cdot}$) or $Fe^{3+}{}_{Si}H$ ($Fe'_{Si} + OH^{\cdot}$) defect configurations rather than the magnesium site of $Al_{Mg}H$ ($V''_{Mg} + Al^{\cdot}_{Mg} + OH^{\cdot}$) or $Fe^{3+}{}_{Mg}H$ ($V''_{Mg} + Fe^{\cdot}_{Mg} + OH^{\cdot}$). We have also calculated the elasticity property of hydrous Brg and PPv. The incorporation of hydrogen in the minerals reduces their K, G moduli and V_P, V_S. However the bulk sound velocities (V_Φ) are rather insensitive to the presence of hydrogen. The effect of hydration onto the elasticity properties is more noticeable in the Fe-bearing system than (Al, Fe)-free or Al-bearing system. In the V_S contrast (dV_S) calculations, it is concluded that the presence of coupled Fe and hydrogen would yield an S-wave anomaly that is very close to the average anomaly value of LLSVPs. This result implies the Fe-bearing hydrous $MgSiO_3$ is likely a dominated mineral in LLSVPs. The thermo-elasticity studies need to be conducted to constrain the thermal effect on the wave velocity of hydrous silicates. The density functional perturbation theory (DFPT) and QHA calculations have been employed to determine the P–T phase diagram of hydrous $Mgsio_3$ minerals and the hydration effect to their phase transition. It is found that hydrogen in the Mg site raise the phase transition boundary to deeper regions in the lower mantle, and the hydrogen, which is substituted at the Si site, will lower the phase transition boundary to shallow parts.

Acknowledgements

We thank two anonymous reviewers for their constructive comments that greatly improved the manuscript. JJ thanks Dr. Joshua Muir for the fruitful discussion. This work was supported by the Hundred Talent Program of the Chinese Academy of Sciences (CAS), China National Thousand (Young) Talents plan, National Natural Science Foundation of China (41773057), with computational resources from Computer Simulation Labs of IGGCAS and USTS, the National Supercomputer Center in Shenzhen, China.

Appendix A. Supplementary material

Supplementary material related to this article can be found online at https://doi.org/10.1016/j.epsl.2019.115753.

References

Blanchard, M., Balan, E., Wright, K., 2009. Incorporation of water in iron-free ringwoodite: a first-principles study. Am. Mineral. 94, 83–89.
Bolfan-Casanova, N., Keppler, H., Rubie, D.C., 2003. Water partitioning at 660 km depth and evidence for very low water solubility in magnesium silicate perovskite. Geophys. Res. Lett. 30, 4.
Brown, J.M., Shankland, T.J., 1981. Thermodynamic parameters in the Earth as determined from seismic profiles. Geophys. J. R. Astron. Soc. 66, 579–596.
Chang, Y.Y., Jacobsen, S.D., Bina, C.R., Thomas, S.M., Smyth, J.R., Frost, D.J., Ballaran, T.B., McCammon, C.A., Hauri, E.H., Inoue, T., Yurimoto, H., Meng, Y., Dera, P., 2015. Comparative compressibility of hydrous wadsleyite and ringwoodite: effect of H_2O and implications for detecting water in the transition zone. J. Geophys. Res., Solid Earth 120, 8259–8280.
Cobden, L., Thomas, C., Trampert, J., 2015. Seismic detection of post-perovskite inside the Earth. In: Khan, A., Deschamps, F. (Eds.), The Earth's Heterogeneous Mantle: A Geophysical, Geodynamical, and Geochemical Perspective. Springer International Publishing, Cham, pp. 391–440.
Deschamps, F., Cobden, L., Tackley, P.J., 2012. The primitive nature of large low shear-wave velocity provinces. Earth Planet. Sci. Lett. 349–350, 198–208.
Dorfman, S.M., Meng, Y., Prakapenka, V.B., Duffy, T.S., 2013. Effects of Fe-enrichment on the equation of state and stability of (Mg, Fe)SiO_3 perovskite. Earth Planet. Sci. Lett. 361, 249–257.
Fiquet, G., Auzende, A.L., Siebert, J., Corgne, A., Bureau, H., Ozawa, H., Garbarino, G., 2010. Melting of peridotite to 140 gigapascals. Science 329, 1516–1518.
Ford, S.R., Garnero, E.J., McNamara, A.K., 2006. A strong lateral shear velocity gradient and anisotropy heterogeneity in the lowermost mantle beneath the southern Pacific. J. Geophys. Res., Solid Earth 111, 14.
Fukui, H., Yoneda, A., Nakatsuka, A., Tsujino, N., Kamada, S., Ohtani, E., Shatskiy, A., Hirao, N., Tsutsui, S., Uchiyama, H., Baron, A.Q.R., 2016. Effect of cation substitution on bridgmanite elasticity: a key to interpret seismic anomalies in the lower mantle. Sci. Rep. 6, 10.
Garnero, E.J., McNamara, A.K., 2008. Structure and dynamics of Earth's lower mantle. Science 320, 626–628.
Gonnermann, H.M., Mukhopadhyay, S., 2007. Non-equilibrium degassing and a primordial source for helium in ocean-island volcanism. Nature 449, 1037–1040.
Gonze, X., Lee, C., 1997. Dynamical matrices, born effective charges, dielectric permittivity tensors, and interatomic force constants from density-functional perturbation theory. Phys. Rev. B 55, 10355–10368.
Hallis, L.J., Huss, G.R., Nagashima, K., Taylor, G.J., Halldorsson, S.A., Hilion, D.R., Mottl, M.J., Meech, K.J., 2015. Evidence for primordial water in Earth's deep mantle. Science 350, 795–797.
He, Y.M., Wen, L.X., 2012. Geographic boundary of the "Pacific Anomaly" and its geometry and transitional structure in the north. J. Geophys. Res., Solid Earth 117, 16.
Hernández, E.R., Alfè, D., Brodholt, J., 2013. The incorporation of water into lower-mantle perovskites: a first-principles study. Earth Planet. Sci. Lett. 364, 37–43.
Inoue, T., Wada, T., Sasaki, R., Yurimoto, H., 2010. Water partitioning in the Earth's mantle. Phys. Earth Planet. Inter. 183, 245–251.
Ishii, M., Tromp, J., 1999. Normal-mode and free-air gravity constraints on lateral variations in velocity and density of Earth's mantle. Science 285, 1231.
Ishii, M., Tromp, J., 2004. Constraining large-scale mantle heterogeneity using mantle and inner-core sensitive normal modes. Phys. Earth Planet. Inter. 146, 113–124.
Keppler, H., Bolfan-Casanova, N., 2006. Thermodynamics of water solubility and partitioning. In: Water in Nominally Anhydrous Minerals, vol. 62, pp. 193–230.
Kresse, G., Furthmuller, J., 1996. Efficient iterative schemes for ab initio total-energy calculations using a plane-wave basis set. Phys. Rev. B 54, 11169–11186.
Kresse, G., Joubert, D., 1999. From ultrasoft pseudopotentials to the projector augmented-wave method. Phys. Rev. B 59, 1758–1775.
Lay, T., Garnero, E.J., 2011. Deep mantle seismic modeling and imaging. In: Jeanloz, R., Freeman, K.H. (Eds.), Annu. Rev. Earth Planet. Sci. 39, 91–123. Annual Reviews, Palo Alto.
Li, L., Brodholt, J.P., Stackhouse, S., Weidner, D.J., Alfredsson, M., Price, G.D., 2005. Elasticity of (Mg, Fe) (Si, Al)O_3-perovskite at high pressure. Earth Planet. Sci. Lett. 240, 529–536.
Litasov, K., Ohtani, E., Langenhorst, F., Yurimoto, H., Kubo, T., Kondo, T., 2003. Water solubility in Mg-perovskites and water storage capacity in the lower mantle. Earth Planet. Sci. Lett. 211, 189–203.
Mao, W.L., Shen, G., Prakapenka, V.B., Meng, Y., Campbell, A.J., Heinz, D.L., Shu, J., Hemley, R.J., Mao, H.-k., 2004. Ferromagnesian postperovskite silicates in the D″ layer of the Earth. Proc. Natl. Acad. Sci. USA 101, 15867–15869.
Monkhorst, H.J., Pack, J.D., 1976. Special points for Brillouin-zone integrations. Phys. Rev. B 13, 5188–5192.
Muir, J.M.R., Brodholt, J.P., 2015. Elastic properties of ferrous bearing $MgSiO_3$ and their relevance to ULVZs. Geophys. J. Int. 201, 496–504.
Muir, J.M.R., Brodholt, J.P., 2018. Water distribution in the lower mantle: implications for hydrolytic weakening. Earth Planet. Sci. Lett. 484, 363–369.
Murakami, M., Hirose, K., Kawamura, K., Sata, N., Ohishi, Y., 2004. Post-perovskite phase transition in $MgSiO_3$. Science 304, 855–858.
Murakami, M., Hirose, K., Sata, N., Ohishi, Y., 2005. Post-perovskite phase transition and mineral chemistry in the pyrolitic lowermost mantle. Geophys. Res. Lett. 32, 4.
Murakami, M., Hirose, K., Yurimoto, H., Nakashima, S., Takafuji, N., 2002. Water in Earth's lower mantle. Science 295, 1885–1887.
Nowacki, A., Wookey, J., Kendall, J.M., 2010. Deformation of the lowermost mantle from seismic anisotropy. Nature 467, 1091–1095.
Oganov, A.R., Ono, S., 2004. Theoretical and experimental evidence for a post-perovskite phase of $MgSiO_3$ in Earth's D″ layer. Nature 430, 445–448.
Ohta, K., Hirose, K., Lay, T., Sata, N., Ohishi, Y., 2008. Phase transitions in pyrolite and MORB at lowermost mantle conditions: implications for a MORB-rich pile above the core–mantle boundary. Earth Planet. Sci. Lett. 267, 107–117.
Panero, W.R., Pigott, J.S., Reaman, D.M., Kabbes, J.E., Liu, Z.X., 2015. Dry (Mg, Fe)SiO_3 perovskite in the Earth's lower mantle. J. Geophys. Res., Solid Earth 120, 894–908.
Pearson, D.G., Brenker, F.E., Nestola, F., McNeill, J., Nasdala, L., Hutchison, M.T., Matveev, S., Mather, K., Silversmit, G., Schmitz, S., Vekemans, B., Vincze, L., 2014. Hydrous mantle transition zone indicated by ringwoodite included within diamond. Nature 507, 221.
Perdew, J.P., Burke, K., Ernzerhof, M., 1996. Generalized gradient approximation made simple. Phys. Rev. Lett. 77, 3865–3868.
Sun, N., Wei, W., Han, S., Song, J., Li, X., Duan, Y., Prakapenka, V.B., Mao, Z., 2018. Phase transition and thermal equations of state of (Fe, Al)-bridgmanite and post-perovskite: implication for the chemical heterogeneity at the lowermost mantle. Earth Planet. Sci. Lett. 490, 161–169.
Tateno, S., Hirose, K., Sata, N., Ohishi, Y., 2005. Phase relations in $Mg_3Al_2Si_3O_{12}$ to 180 GPa: effect of Al on post-perovskite phase transition. Geophys. Res. Lett. 32, 4.
Togo, A., Chaput, L., Tanaka, I., Hug, G., 2010. First-principles phonon calculations of thermal expansion in Ti_3SiC_2, Ti_3AlC_2, and Ti_3GeC_2. Phys. Rev. B 81.
Townsend, J.P., Tsuchiya, J., Bina, C.R., Jacobsen, S.D., 2015. First-principles investigation of hydrous post-perovskite. Phys. Earth Planet. Inter. 244, 42–48.

Townsend, J.P., Tsuchiya, J., Bina, C.R., Jacobsen, S.D., 2016. Water partitioning between bridgmanite and postperovskite in the lowermost mantle. Earth Planet. Sci. Lett. 454, 20–27.

Trampert, J., Deschamps, F., Resovsky, J., Yuen, D., 2004. Probabilistic tomography maps chemical heterogeneities throughout the lower mantle. Science 306, 853.

Tsuchiya, T., Tsuchiya, J., 2006. Effect of impurity on the elasticity of perovskite and postperovskite: velocity contrast across the postperovskite transition in (Mg, Fe, Al)(Si, Al)O_3. Geophys. Res. Lett. 33, 4.

Tsuchiya, T., Tsuchiya, J., Umemoto, K., Wentzcovitch, R.M., 2004. Phase transition in $MgSiO_3$ perovskite in the Earth's lower mantle. Earth Planet. Sci. Lett. 224, 241–248.

Wang, W.Z., Walter, M.J., Peng, Y., Redfern, S., Wu, Z.Q., 2019a. Constraining olivine abundance and water content of the mantle at the 410-km discontinuity from the elasticity of olivine and wadsleyite. Earth Planet. Sci. Lett. 519, 1–11.

Wang, X.L., Tsuchiya, T., Zeng, Z., 2019b. Effects of Fe and Al incorporations on the bridgmanite–postperovskite coexistence domain. C. R. Geosci. 351, 141–146.

Wicks, J.K., Jackson, J.M., Sturhahn, W., 2010. Very low sound velocities in iron-rich (Mg, Fe)O: implications for the core–mantle boundary region. Geophys. Res. Lett. 37, 5.

Wright, K., 2006. Atomistic models of OH defects in nominally anhydrous minerals. In: Water in Nominally Anhydrous Minerals, vol. 62, pp. 67–83.

Zhang, F., Oganov, A.R., 2006a. Mechanisms of Al^{3+} incorporation in $MgSiO_3$ postperovskite at high pressures. Earth Planet. Sci. Lett. 248, 69–76.

Zhang, F., Oganov, A.R., 2006b. Valence state and spin transitions of iron in Earth's mantle silicates. Earth Planet. Sci. Lett. 249, 436–443.

Zhang, Z., Dorfman, S.M., Labidi, J., Zhang, S., Li, M., Manga, M., Stixrude, L., McDonough, W.F., Williams, Q., 2016. Primordial metallic melt in the deep mantle. Geophys. Res. Lett. 43, 3693–3699.

Zhang, Z.G., Stixrude, L., Brodholt, J., 2013. Elastic properties of $MgSiO_3$-perovskite under lower mantle conditions and the composition of the deep Earth. Earth Planet. Sci. Lett. 379, 1–12.